Deep–Sea Research I 186 (2022) 103828

Contents lists available at ScienceDirect

Deep-Sea Research Part I

journal homepage: www.elsevier.com/locate/dsri

Modulation of submesoscale motions due to tides and a shallow ridge along the Kuroshio

Eiji Masunaga [a,b,*], Yusuke Uchiyama [c], Xu Zhang [d], Waku Kimura [e], Taichi Kosako [f]

[a] Global and Local Environment Co-creation Institute, Ibaraki University, Japan
[b] Scripps Institution of Oceanography, University of California, San Diego, La Jolla, CA, USA
[c] Department of Civil Engineering, Kobe University, Japan
[d] Department of Atmospheric and Oceanic Sciences, School of Physics, Peking University, China
[e] Kajima Corporation, Japan
[f] Port and Airport Research Institute, Japan

ARTICLE INFO

Keywords:
Submesoscale motions
Kuroshio
Tides
Kinetic energy budget
The Izu-Ogasawara ridge

ABSTRACT

This study investigated submesoscale motions (SMs) and transport over the Izu-Ogasawara Ridge, located off mainland Japan, using a double-nested Regional Oceanic Modeling System (ROMS). Both the Kuroshio and tides largely influence physical processes in this area. The mean and submesoscale kinetic energies (MKE and SKE, respectively) were calculated using a horizontal Gaussian filter. Tidal forcing enhances SKE through Reynolds stress due to mean velocity shear (barotropic conversion); meanwhile, tides suppress the MKE and total kinetic energy. This implies that tidal forcing contributes to energy transfer from large-scale motions to smaller scales, which results in accelerated kinetic energy dissipation. Energy conversion from submesoscale potential energy to SKE (baroclinic conversion) is reduced by tidal forcing. In the summer, SKE is generated by barotropic conversion and suppressed by negative baroclinic conversion. On the other hand, in winter, SKE is enhanced by both barotropic and baroclinic conversions.

1. Introduction

The Kuroshio Current ('the Kuroshio') is a western boundary current and a major source of kinetic energy that significantly contributes to ocean circulation and ecosystems in the northwestern Pacific Ocean (e.g., Guo et al., 2013; Kodama et al., 2014). The Kuroshio flows from the southwest toward the east of mainland Japan, and its flow magnitude and transport volume reach 2.0 m s^{-1} and 65 Sv (1 Sv = 10^6 m^3 s^{-1}), respectively (Andres et al., 2015) . Several shallow straits and ridges are located along the Kuroshio path, including the Tokara Strait and Izu-Ogasawara Ridge (Fig. 1). Instability and strong mixing occur when the Kuroshio passes over shallow regions (e.g., Hasegawa et al., 2004; Nagai et al., 2017; Tsutsumi et al., 2017). Observations conducted by Hasegawa et al. (2004) showed strongly enhanced mixing due to the Kuroshio passing around an island, leading to upwelling of deep plankton-rich water. Tsutsumi et al. (2017) reported that an interaction between the Kuroshio and a shallow ridge resulted in near-inertial internal waves accompanied by strong diapycnal mixing. The Kuroshio also transports fish larvae from tropical oceans toward mid-latitude coastal regions (e.g., Chang et al., 2018; Miyake et al., 2020), and Miyake et al. (2020) showed that the catch of glass eels increases as the Kuroshio path shifts toward the coast.

Oceanic eddying motions are typically categorized into two scales: (1) mesoscale motions with horizontal scales of O (100) km or larger and (2) submesoscale motions (SMs) with horizontal scales of less than tens of kilometers. SMs with scales of O (0.1–10) km include eddies, filaments, and fronts, and are referred to as submesoscale coherent structures (e.g., McWilliams, 2016; Dauhajre and McWilliams, 2018). Recently developed high-resolution observational techniques and numerical simulations can resolve SMs, and these approaches have revealed the importance of SMs in energy transports/cascades and mass transport (e.g., Thomas et al., 2008; McWilliams, 2016). SMs are dynamically defined by the Rossby number, $R_o > O(1)$ ($R_o = U/fL$, where U is the velocity, f is the Coriolis parameter, and L is the length scale) (Thomas et al., 2008); that is, SMs are not bounded by the Earth's rotational effect. The vertical length and time scales of SMs range from approximately 10 to 1000 m and less than several days, respectively (McWilliams, 2016). SMs are accompanied by intensified vertical

* Corresponding author. Global and Local Environment Co-creation Institute, Ibaraki University, 4-12-1, Nakanarusawa, Hitachi, Ibaraki, Japan.
E-mail address: eiji.masunaga.office@vc.ibaraki.ac.jp (E. Masunaga).

https://doi.org/10.1016/j.dsr.2022.103828
Received 19 July 2021; Received in revised form 7 June 2022; Accepted 17 June 2022
Available online 20 June 2022

motion in the surface mixed layer, which significantly contributes to vertical mass and heat fluxes (Su et al., 2018). The vertical flux due to SMs is occasionally larger than that caused by mesoscale eddies and turbulent mixing (e.g., Mahadevan, 2016). Importantly, the upward nutrient flux associated with SMs contributes to maintaining primary production in the surface layers (e.g., Lévy et al., 2012; Uchiyama et al., 2017), and submesoscale eddy-driven subduction transports organic carbon from surface layers toward the deep oceans (Omand et al., 2015).

Mesoscale motions and SMs are present in the vicinity of the Kuroshio path (e.g., Waseda et al., 2003; Sasaki et al., 2014; Uchiyama et al., 2017). The Kuroshio, accompanied by large mesoscale cyclonic eddies, induces upwelling, which intensifies primary production in the upper ocean (e.g., Kimura et al., 1997). High-resolution numerical simulations by Sasaki et al. (2014) showed enhanced SMs in the surface mixed layer due to baroclinic instability, referred to as mixed-layer instability (Boccaletti et al., 2007), in the winter season. Uchiyama et al. (2017) found that the SMs induce vertical nutrient supply and promote primary production in the Kuroshio extension. Yang et al. (2021a) reported two major processes for generating SM-induced vertical heat transport: geostrophic deformation and vertical mixing of momentum in the Kuroshio extension. In addition to vertical transport, Kamidaira et al. (2017) suggested that SMs significantly contribute to lateral heat transport from the Kuroshio toward the coast in the vicinity of the Ryukyu Islands.

In addition to mesoscale currents and SMs, tides significantly contribute to ocean dynamics and transport. Interaction between topography and barotropic tides generates internal waves (e.g., Alford et al., 2015; Masunaga et al., 2019) and SMs (e.g., Nakamura et al., 2012; Cheng et al., 2020). The typical lateral wave phase speed of internal tides is of the order of 1 m s^{-1}. Assuming a wave speed of 1 m s^{-1} and a wave period of M2 (12.42 h), the horizontal wavelength is approximately 45 km, which is within the range of the submesoscale. Nonlinear internal tides exhibit small-scale physical processes with horizontal scales of less than *O* (10) km (Masunaga et al., 2019b). Rocha et al. (2016) also suggested that internal tides influence mesoscale and submesoscale dynamics in the upper ocean in the Kuroshio extension. Nakamura et al. (2012) reported SMs generated by barotropic tides around islands near the Kuril Strait, based on satellite images and numerical simulations. Furthermore, numerical simulations conducted by Cheng et al. (2020) showed that SMs generated by the Kuroshio at a sharp cape, located south of Taiwan, are modulated by tidal flows. While tides may contribute to the generation of SMs, tidally generated SMs are not well understood.

This study examines the physical processes and transport associated with SMs around a shallow ridge, the Izu Ogasawara Ridge (Fig. 1), where both the Kuroshio and tides have a significant influence. Numerical simulations conducted by Masunaga et al. (2018) showed that 67%, 20%, and 13% of the total kinetic energy over the northern area of this ridge is generated by the Kuroshio, tides, and wind stress, respectively. SMs are enhanced by the Kuroshio flow over the ridge owing to lateral mean shear stress (Uchiyama et al., 2017). In addition, numerous islands are located along the Kuroshio path and von Karman vortex-like SMs are generated in island wakes (Liu and Chang, 2018). An interaction between bathymetry and barotropic tides generates strong internal tides that propagate from the ridge (Varlamov et al., 2015; Masunaga et al., 2018). Diurnal internal tides are trapped around islands located on ridges, leading to vertical mixing and lateral mass transport (Masunaga et al., 2020). Masunaga et al. (2019) found that an interaction between the background Kuroshio and tides strongly enhance internal wave propagation toward the Kuroshio downstream.

We employed a double-nested Regional Oceanic Modeling System (ROMS; Shchepetkin and McWilliams, 2005) with a horizontal grid resolution of 1 km to investigate SMs in the study area; this is an appropriate resolution for simulating submesoscale dynamics and associated transport processes in the upper ocean (e.g., Capet et al., 2008; Kamidaira et al., 2018). It is well known that submesoscale dynamics vary seasonally (Sasaki et al., 2014; Uchiyama et al., 2017). Tides and internal tides significantly influence the kinetic energy in deep layers (depth >1000 m; Kang and Fringer, 2012; Masunaga et al., 2017, 2020). In this study, we present a full-depth kinetic energy budget analysis associated with SMs for two seasons and two forcing cases, summer and winter, with and without tidal forcing. The remainder of this paper is organized as follows. Section 2 describes the configuration and validation of the proposed model. Section 3 presents the background physical conditions, submesoscale kinetic energy (SKE) budget, and generation mechanism of SKE Finally, section 4 summarizes the study and presents the main conclusions.

2. Model configuration

2.1. ROMS model

We employed a double-nested ROMS covering the northern area of the Izu-Ogasawara Ridge (Fig. 1a and b). The outer nested domain (L1) of the ROMS was embedded in the 7-year-averaged daily climatological oceanic data (2008–2014) obtained from the JCOPE2 reanalysis product (Miyazawa et al., 2009). The horizontal resolution was 3 km, and 32 vertical *s*-coordinate layers were used for the L1 domain (see Uchiyama et al., 2017 for more details on L1 model configuration). The inner domain (L2), with a horizontal grid spacing of 1 km, was nested in the parent L1 model using the one-way offline nesting method proposed by Mason et al. (2010). Vertical *S-coordinates* with 40 layers were used for vertical gridding. The model topography was derived from the J-EGG500 (Japan Oceanographic Data Center) and SRTM30_PLUS (Becker et al., 2009) products. The open boundaries were forced by horizontal currents, tracers (temperature and salinity), and sea surface height from the parent L1 model output after a 1-year spin-up. Barotropic (BT) tidal forcing was also imposed at the L2 open boundaries using the TPXO 7.0 tidal constituents (Egbert and Erofeeva, 2002). The

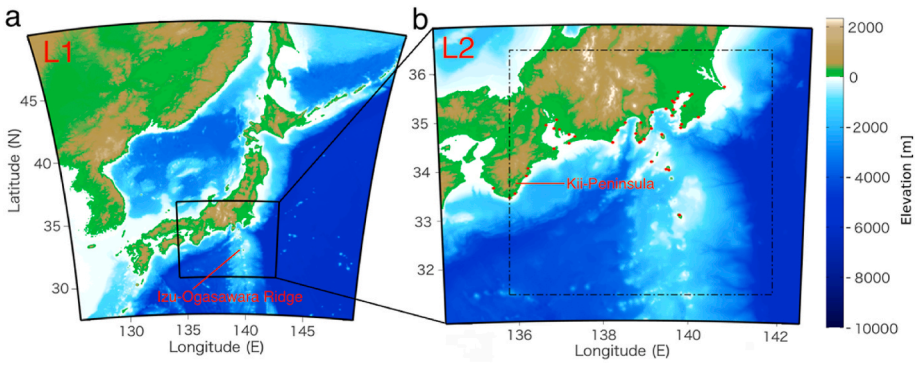

Fig. 1. Maps of the model domains of the (a) parent L1 and (b) downscaled L2. The red dots show the locations of tidal gauge stations used for model validation. The black chain-dotted box in panel (b) is the analysis area for this study.

amplitude and phase of the TPXO tide model were slightly modified to improve the reproducibility of tidal signals (see Masunaga et al., 2018). The ocean surface boundary condition was imposed using the daily climatological grid point value of the global spectral model (GPV-GSM) product (Japan Meteorological Agency, JMA; e.g., Roads, 2004) for wind, and monthly climatological surface heat, freshwater fluxes, and radiation fluxes from the NOAA-COADS dataset (Woodruff et al., 1987). Freshwater discharge from 31 rivers was also imposed using monthly averaged climatological data provided by the Japan River Association (http://www.japanriver.or.jp/publish/book/nenpyou_dvd.htm). Vertical eddy viscosity and diffusivity were estimated using the K-Profile Parameterization (KPP) mixed-layer turbulence model (Large et al., 1994). The horizontal eddy viscosity and diffusivity were set to 0 $m^2 s^{-1}$, and the baroclinic (BC) time step was set to 10 s.

To investigate the effects of background geostrophic flows (i.e., the Kuroshio), tides, and seasonal variations, four model runs were conducted: summer without tides (Run #1), summer with tides (Run #2), winter without tides (Run #3), and winter with tides (Run #4). The model cases with and without tides allowed us to discriminate the effects of tides/internal tides and evaluate the effects of tidal forcing. The L2 model was spun-up approximately 1 and 1.5 years without tidal forcing for the winter and summer runs, respectively. The analysis period was set to 28 days (i.e., approximately two spring–neap tidal cycles) in all cases, and the days with the warmest and coldest water temperatures were set in the middle of the summer and winter periods, respectively. Tidal forcing was imposed 14 days prior to the analysis period, and the hourly averaged model outputs were used in subsequent analyses.

2.2. Validation of the ROMS model

It has been reported that double-nested ROMS-L1 and L2 model results show good agreement with field observations around the Kuroshio stream (Kamidaira et al., 2017; Uchiyama et al., 2018). Snapshots of the surface temperature and velocity magnitude from the L2 model are plotted on those from the parent L1 model for both summer and winter cases in Fig. 2. The warm Kuroshio water flowing into the western boundary and out of the eastern boundary is well downscaled to the L2 domain from the L1 domain. Large temperature and velocity gaps are not observed between the L2 and L1 models. Therefore, we assume that the double-nested L2 model is successfully nested in the parent L1 model. Validations of the outer L1 domain have been reported by Uchiyama et al. (2017).

The amplitude and phase of the four tidal constituents (S2, M2, K1, and O1) between our model and those provided by the JMA for 43 tidal gauge stations are compared in Fig. 3 (the locations of the tidal gauge

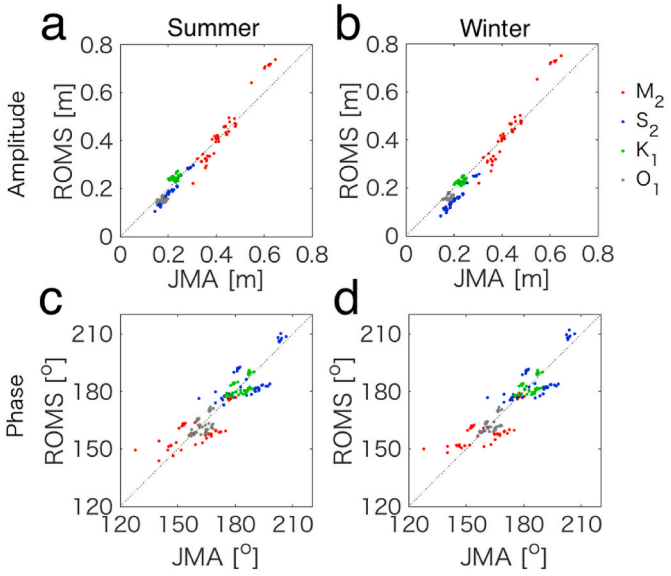

Fig. 3. Model validation for the four principle tidal constituents. S2 (blue), M2 (red), K1 (green), and O1 (gray); (a, b) amplitude and (c, d) phase for (a, c) summer and (b, d) winter.

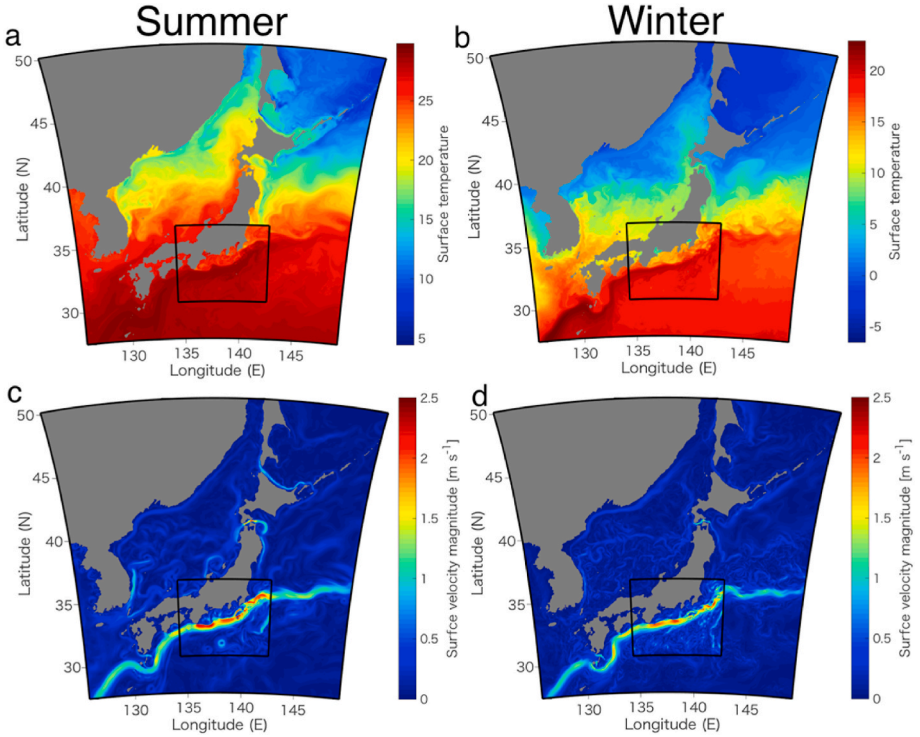

Fig. 2. Snapshots of L2 model results on those from the L1 parent model at the midpoint of the analysis periods. (a, b) Surface temperature; and (c, d) surface velocity magnitude for (a, c) summer and (b, d) winter.

stations are shown as red dots in Fig. 1b). The root-mean-square error (E) between the modeled and observed tidal constituents is given by the following formula (Carter et al., 2008):

$$E = \sqrt{\frac{1}{2}(a_O^2 + a_M^2) - a_O a_M \cos(G_O - G_M)} \quad (1)$$

where a is the amplitude of the tides, G is the tidal phase, and the subscripts O and M denote the values of the observational constant from the JMA and our model, respectively. The resulting error is less than 5.4×10^{-2} m, and the averaged error over the four tidal constituents is computed as 2.9×10^{-2} and 3.1×10^{-2} m for summer and winter, respectively (Table 1). The average relative errors (E/a_O) for the summer and winter cases are 11% and 12%, respectively.

3. Results and discussion

3.1. Background physical conditions

The time-averaged surface temperatures and velocities from the model cases without tidal forcing (Runs #1 and #3) are plotted in Fig. 4. The surface temperature along the Kuroshio axis is approximately 10 °C higher in summer than in winter; however, the horizontal temperature gradient is consistent in both cases. The Kuroshio passes over the Izu-Ogasawara Ridge with a maximum velocity magnitude exceeding 2 m s^{-1} and is separated into several branches due to the presence of islands (Fig. 4c and d, branches are clearer in the summer case). The inflow rates of the Kuroshio at the western boundary are approximately 54 and 55 Sv (1 Sv = 10^6 m^3 s^{-1}) for the summer and winter cases, respectively. The Kuroshio path is broadly consistent between the summer and winter seasons in the upstream region (136°E–139°E). However, the Kuroshio tends to pass over the northern area of the ridge during summer. The surface velocity along the Kuroshio is slightly lower in winter than in summer because the surface mixed layer deepens in winter, resulting in deceleration of the flow magnitude in the surface layer. A cyclonic eddy exists along the coast upstream of the Kuroshio (34°N, 137°E–139°E) in both summer and winter, which has been frequently observed in previous studies (e.g., Nakata et al., 2000; Uchiyama et al., 2017). Two additional model cases with tidal forcing (Runs #2 and #4) also exhibit background conditions that are similar to the results shown in Fig. 4 (Runs #1 and #3), indicating that tidal forcing does not largely influence the background conditions.

The surface relative vorticity, ζ/f, is plotted in Fig. 5a and b, where $\zeta = \partial v/\partial x - \partial u/\partial y$ and f is the Coriolis frequency. In particular, in winter, small-scale eddies with $\zeta/f > 1$ occur across the entire model domain. Topography–current-generated vortices and filaments also appear near the coast and in island wakes on the Kuroshio downstream during both seasons. Horizontal kinetic energy spectra were computed for the four model cases (Runs #1–4) from the horizontal velocity components (u and v) obtained along the 32.3°E latitude line (Fig. 5c), shown as black chain-dotted lines in Fig. 5a and b. The power of the spectra where the wavenumber is higher than 10^{-5} cpm and is approximately one order of magnitude higher in winter than in summer. Tidal forcing slightly enhances and suppresses the power at higher wavenumbers in summer and winter in the presence of tidal forcing, respectively. This indicates that SMs are enhanced and suppressed at 32.3°E in summer and winter, respectively. This seasonal variation in effects of tidal forcing is consistent with previously reported SMs in the Kuroshio Extension (Rocha et al., 2016). The kinetic energy spectra follow a slope of −2 in the fully developed submesoscale turbulent regime (Capet et al., 2008; Kamidaira et al., 2018). The kinetic energy spectra are close to a slope of −2 in winter and close to a slope of −3 in summer (Fig. 5c) Therefore, fully developed SMs are established for winter cases.

Table 1
Root-mean-square error (E) between modeled tidal elevations and tidal constants provided by the Japan Meteorological Agency.

	Summer	Winter
	E [m]	E [m]
M2	5.2×10^{-2}	5.4×10^{-2}
S2	2.6×10^{-2}	4.2×10^{-2}
K1	1.8×10^{-2}	1.4×10^{-2}
O1	2.1×10^{-2}	1.6×10^{-2}
Average	2.9×10^{-2}	3.1×10^{-2}

3.2. Extraction of SMs

We used a horizontal two-dimensional Gaussian smoothing filter to decompose the submesoscale and mean (or mesoscale) velocities. The filter length scale (standard deviation) and the size of the filter window were set to 9 km and 30 × 30 km, respectively. We refer to the submesoscale and mean velocity components as $\mathbf{u}_S$ and $\mathbf{u}_M$, respectively ($\mathbf{u}_S = \mathbf{u} - \mathbf{u}_M$, $\mathbf{u}_M = \tilde{\mathbf{u}}$, where $\tilde{u}$ indicates the filtered spatial mean velocity with the spatial Gaussian filter). The horizontal kinetic energy spectra computed from $\mathbf{u}_E$ and $\mathbf{u}_M$ for Run #3 are compared in Fig. 5d. The two spectra from $\mathbf{u}_S$ and $\mathbf{u}_M$ cross at 2.2×10^{-5} cpm (with a horizontal scale of approximately 45 km). Thus, $\mathbf{u}_S$ and $\mathbf{u}_M$ dominate the kinetic energy at scales smaller and larger than approximately 45 km, respectively. Although the cutoff wave number/scale cannot be clearly defined when we use the Gaussian filter, the cutoff length scale seems to be approximately 45 km for our case. Snapshots of the relative surface vorticity from the mean (ζ_M/f) and submesoscale (ζ_S/f) velocities are plotted in Fig. 6. The vorticity from submesoscale velocities clearly shows enhanced SMs along the coast of mainland Japan and in the Kuroshio downstream during both seasons, and in the southern area of the model domain in winter (Fig. 6c and d). During the summer season, the submesoscale vorticity shows thin filament-like structures near coastal regions, which are supposed to be partly caused by topographic effects. Although the mean vorticity shows numerous vortices/filaments with scales larger than ~50 km in winter, the intensity of the mean vorticity components is similar for both seasons (Fig. 6a and b).

Table 2 shows the mean square (MS) of the relative vorticity, $\overline{<(\zeta_M/f)^2>}$ and $\overline{<(\zeta_S/f)^2>}$, computed from $\mathbf{u}_M$ and $\mathbf{u}_S$, respectively, for all four model cases (Runs #1–4), where brackets and overbars denote horizontal and time averaging operators, respectively. MS was computed for the entire 28-day analysis period. According to the t-test, differences in the MS of vorticity are significantly different for all model cases ($p < 0.01$), where the t-test compare the time series of the horizontally averaged MS of relative vorticity. The MS of the mean vorticity does not change largely between the model cases, with differences of less than 6%. In comparison, submesoscale vorticity varies owing to seasonal differences and tidal forcing; submesoscale vorticity is found to be approximately twice as high in winter as it is in summer, which is also clearly seen in the vorticity maps (Fig. 6c and d). Furthermore, tidal forcing enhances submesoscale vorticity by 17% during the summer. Thus, the Gaussian filter successfully extracts SMs that are influenced by seasonal variation and tides.

3.3. Submesoscale kinetic energy

The total, mean, and submesoscale kinetic energy (KE, MKE, and SKE) terms are given by

$$KE : K_{Total} = \frac{1}{2}\left(u^2 + v^2 + w^2\right) \quad (2)$$

$$MKE : K_M = \frac{1}{2}\left(u_M^2 + v_M^2 + w_M^2\right) \quad (3)$$

$$SKE : K_S = \frac{1}{2}\left(u_S^2 + v_S^2 + w_S^2\right) \quad (4)$$

Note that the sum of K_M and K_S is not equal to K_{Total} because of the

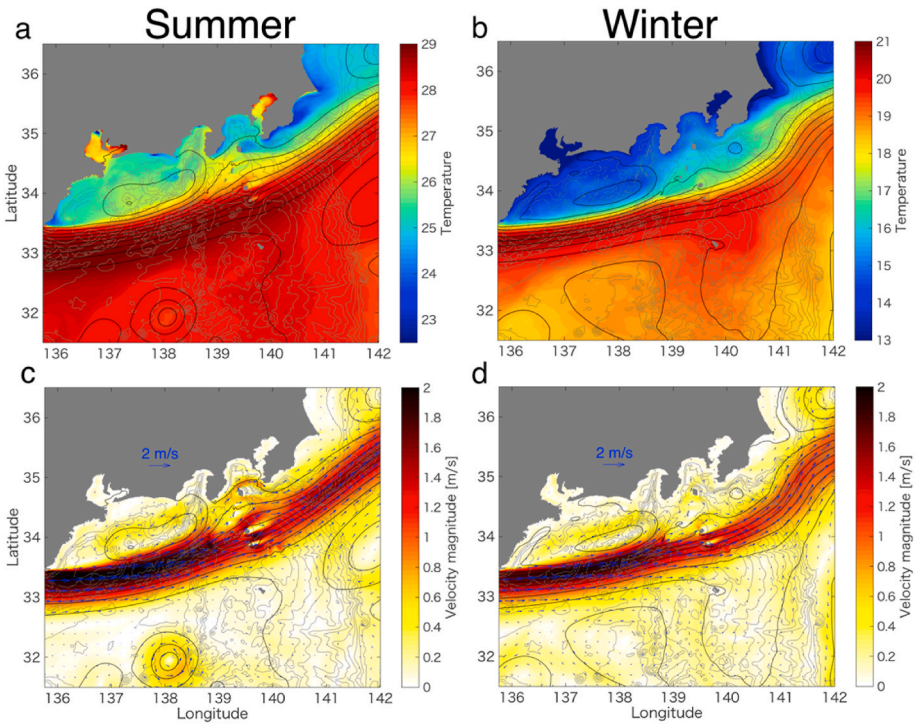

Fig. 4. Time-averaged (a, b) surface temperature and (c, d) surface velocity over the 4-week (28-day) analysis period for (a, c) summer and (b, d) winter. Time averages were obtained for the entire 28-day analysis period. The gray and black contour lines are isobaths at intervals of 500 m and sea-surface height at intervals of 0.1 m, respectively.

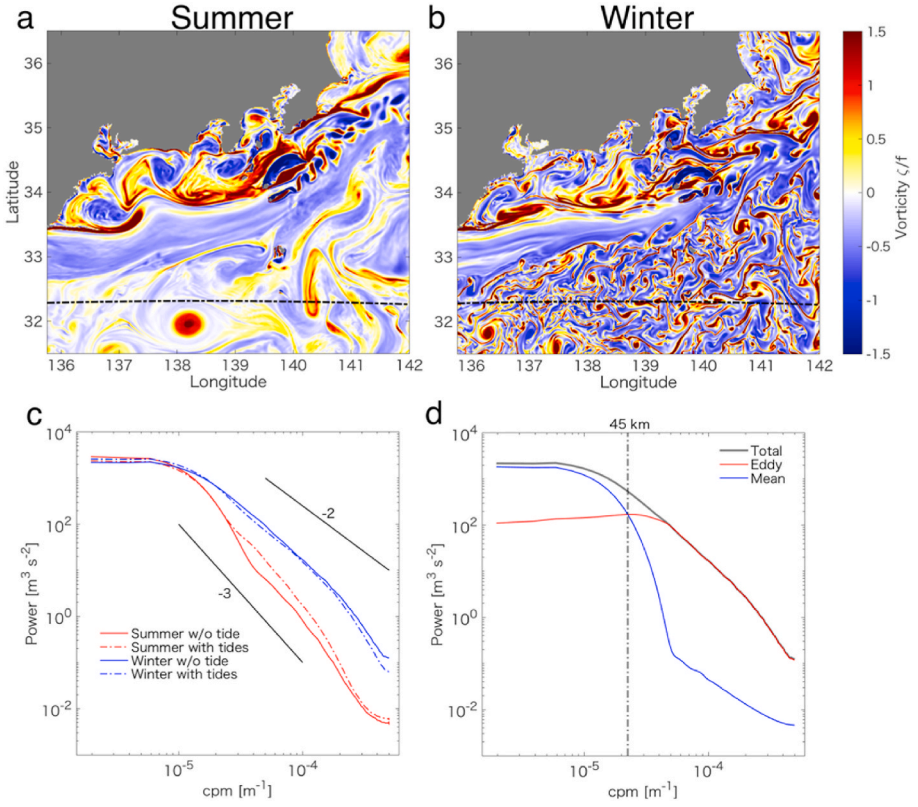

Fig. 5. (a, b) Snapshots of surface relative vorticity for (a) summer and (b) winter, and (c, d) kinetic energy spectra along the black chain-dotted lines in panels (a, b). Panel (d) compares the kinetic energy spectra of mean and submesoscale components extracted using the Gaussian filter for the winter case (Run #3). The kinetic energy spectra are averaged over the 4-week (28-day) analysis period.

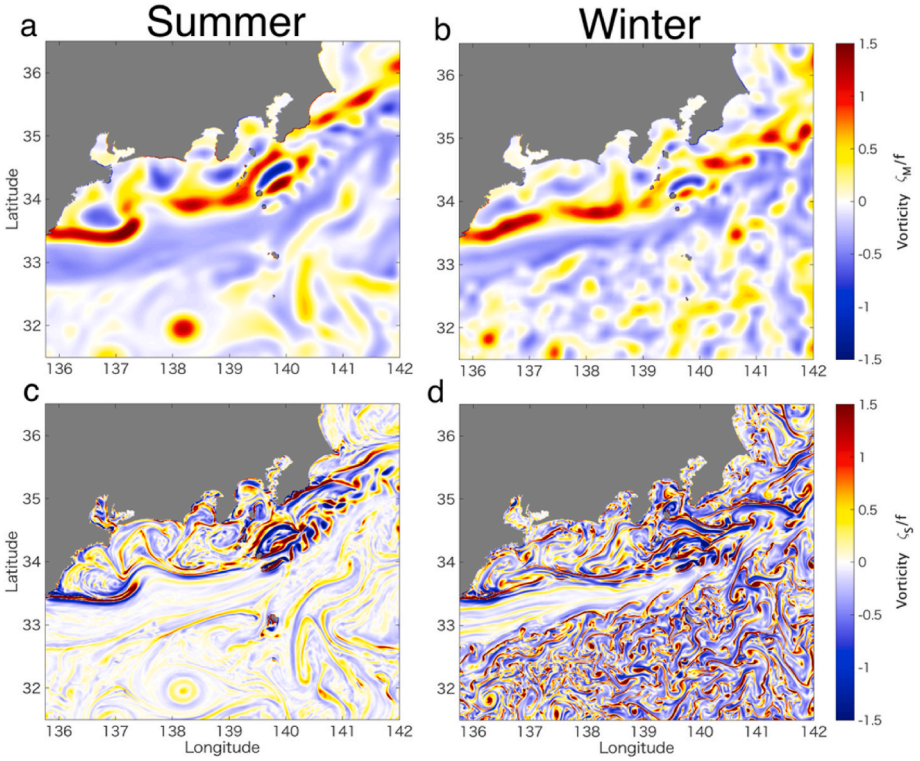

Fig. 6. Snapshots of surface relative vorticity computed from (a,b) mean and (c,d) submesoscale components for the (a,c) summer (Run #1) and (b,d) winter cases (Run #3). The times of these snapshots are the same as those in Fig. 5a and b.

Table 2
Mean square (MS) of relative vorticity in the surface layer for the summer and winter model cases.

	Summer		Winter	
	w/o tides Run #1	with tides Run #2	w/o tides Run #3	with tides Run #4
$\overline{<(\zeta_M/f)^2>}$	8.6×10^{-2}	8.1×10^{-2}	8.4×10^{-2}	8.2×10^{-2}
$\overline{<(\zeta_S/f)^2>}$	2.3×10^{-1}	2.7×10^{-1}	4.7×10^{-1}	5.0×10^{-1}

cross-term K_C ($K_{Total} = K_M + K_S + K_C$, where $K_C = u_M u_S + v_M v_S + w_M w_S$), which is not considered in this study. The time-averaged and depth-integrated KE, MKE, and SKE are shown in Fig. 7a–c and Fig. 8a–c for the summer and winter cases, respectively. In addition, Fig. 7d–f and Fig. 8d–f shows the ratio of kinetic energy between the model cases with and without tidal forcing (i.e., kinetic energy from a model with tidal forcing divided by that without tidal forcing). High KE regions appear along the Kuroshio stream, with the KE reaching $O(10^3)$ m^3 s^{-2} (Figs. 7a and 8a). The MKE shows a distribution similar to that of KE (Fig. 7a and b and Fig. 8a and b), which implies that MKE dominates the total kinetic energy. The SKE is much lower than the MKE (Fig. 7b and c and Fig. 8b and c); the domain-time-averaged and depth-integrated SKE is approximately 8% of the MKE (Table 3). On the other hand, SKE is enhanced over the ridge and is comparable to MKE downstream of the Kuroshio (Figs. 7c and 8c; ~140°E–141°E and 34°N). In the southern area of the model domain, SKE is higher in winter than in summer (Fig. 7b and c and Fig. 8b and c), which probably reflects the enhanced SMs during the winter season, as shown in Fig. 6.

Tides reduce the MKE in the Kuroshio stream and enhance the MKE along the coast and in the vicinity of the islands over the ridge (Figs. 7e and 8e). The area- and time-averaged vertically integrated MKE is suppressed by tidal forcing by 8% and 6% in the summer and winter, respectively (Table 3). The total kinetic energy (KE) is also decreased by tides, similar to that of the MKE. In contrast, the SKE is intensified by tidal forcing by 15% and 13% in summer and winter, respectively (Figs. 7f and 8f, Table 3). These kinetic energies are found to have statistically significant differences based on the *t*-test ($p < 0.01$), which compares the time series of the area-averaged and depth-integrated kinetic energies. These results demonstrate that tidal forcing deaccelerates the Kuroshio and promotes the generation of SKE and dissipation of KE. A significant enhancement of SKE appears in the southwest area of the model domain during the summer season (Fig. 7f; 136°E–13°E and <33°N). It has been reported that internal wave energy increases in summer in the study area owing to highly stratified conditions (Rocha et al., 2016; Masunaga et al., 2020). Enhanced SKE due to tides far from the coast and ridge in our model results might be influenced by internal tides (see Section 3.4).

To further investigate regional-scale variations in kinetic energy, the area- and time-averaged and vertically integrated KE, MKE, and SKE values were computed for the following six regions (Fig. 9, Table 3): (1) coastal upstream (CU), (2) coastal downstream (CD), (3) Kuroshio upstream (KU), (4) Kuroshio downstream (KD), (5) offshore upstream (OU), and (6) offshore downstream (OD). The "coastal", "Kuroshio", and "offshore" regions are defined by time-averaged sea-surface heights of less than −0.1 m, −0.1–0.6 m, and higher than 0.6 m, respectively, for the summer cases. For the winter cases, these three regions are separated by time-averaged sea-surface heights of −0.3 and 0.3 m. The "upstream" and "downstream" regions are separated by a straight line passing the islands positioned on the Izu-Ogasawara Ridge (the line is given by $Lat = -4.4 \times Long + 648.12$, where *Lat* and *Long* are latitude and longitude, respectively, see Fig. 9).

The KU region is the most energetic MKE region, and MKE is reduced by 29% and 40% between the KU and KD regions in summer and winter, respectively (Table 3). Meanwhile, SKE is 2.2 (1.6) times higher in the KD region than in the KU region for summer (winter). Assuming that MKE is mainly transported in the upstream-downstream direction, an interaction between the Kuroshio and ridge results in the dissipation of MKE and energy transfer from MKE to SKE. The differences in kinetic

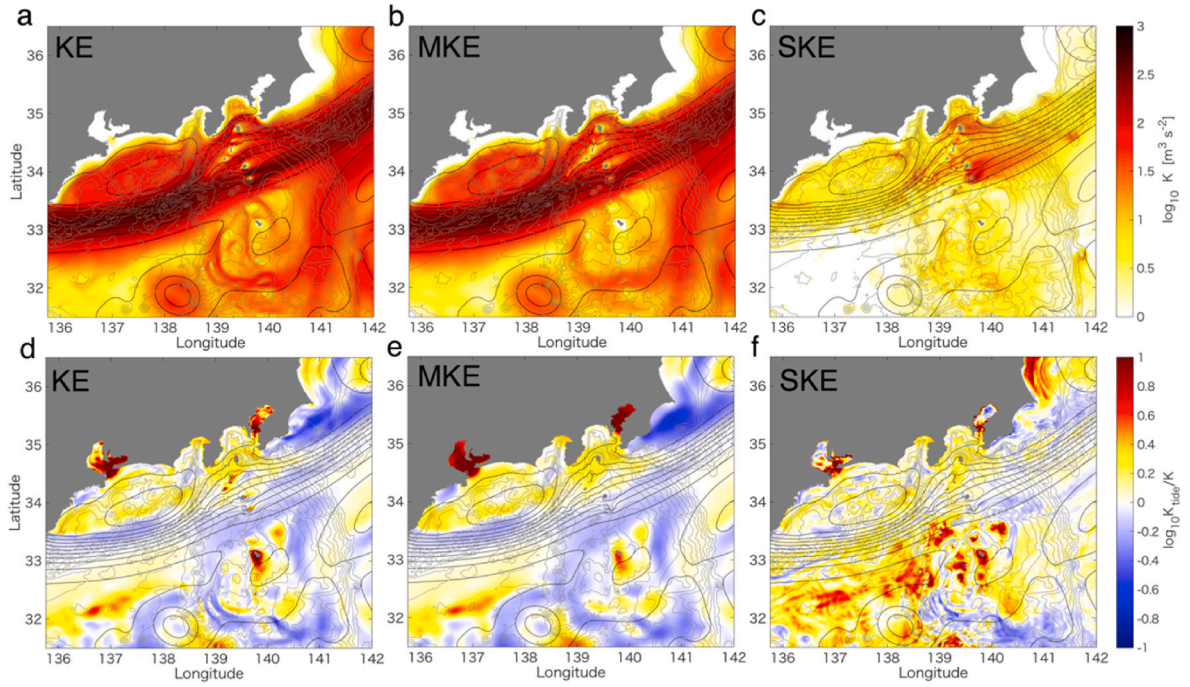

Fig. 7. Time-averaged and depth-integrated (a) total kinetic energy, (b) mean kinetic energy, and (c) submesoscale kinetic energy for the summer model case (Run #1); (d–f) lower panels show the ratio of kinetic energy between model cases with and without tidal forcing (kinetic energy from Run #2 is divided by that from Run #1). Gray and black contour lines are isobaths spaced at intervals of 500 m and iso-sea-surface height at intervals of 0.1 m, respectively.

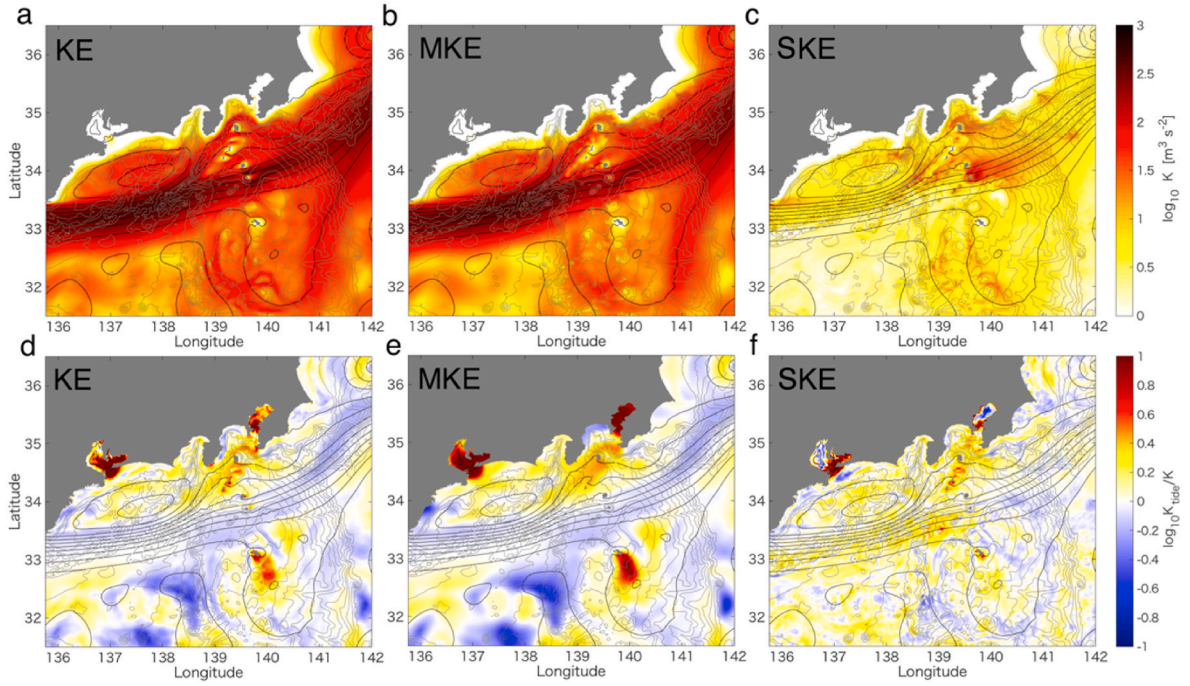

Fig. 8. As for Fig. 7 but for the winter season.

energy between the model cases with and without tidal forcing were validated using the *t*-test. Tidal forcing significantly modulates kinetic energy, except for KE and MKE in the CD region in winter and SKE in the KD and OD regions in winter (Table 3). KE and MKE in the CU (CD) region are enhanced (reduced) by tides during the summer (Table 3). Although both the CU and CD regions are coastal, the effect of tides on kinetic energy varies. The higher KE (or MKE) in the CU region than in the CD region reflects a cyclonic eddy generated along the north side of the Kuroshio (Figs. 4, Figure 7, and Fig. 8) and tidally enhanced KE in the CU region (Table 3), indicating that the CU region is an energetic coastal region largely influenced by both Kuroshio-induced cyclonic eddies and tides. Tidal forcing enhances the SKE, except in the OD region in summer, and the KD and OD regions in winter (Table 3). In particular, SKE is considerably enhanced in the KU by 25% and 37% in summer and winter, respectively.

To further investigate the modulations of kinetic energy due to tidal

Table 3
Area- and time-averaged and depth-integrated kinetic energy for the model runs with tidal forcing (unit of $m^3\ s^{-2}$; Runs #2 and #4). Values in brackets are differences between model cases with and without tidal forcing. Positive and negative values in brackets indicate kinetic energy is increased or decreased by tidal forcing, respectively. Asterisks (*) denote no significant difference between results from models with and without tidal forcing (*t*-test, $p > 0.01$).

	Summer			Winter		
	KE	MKE	SKE	KE	MKE	SKE
All areas	70.3 (−4.5)	60.1 (−4.9)	4.7 (+0.5)	75.2 (−3.4)	64.0 (−3.9)	4.4 (+0.5)
CU	47.6 (+7.8)	36.8 (+5.9)	5.2 (+0.8)	38.9 (+3.0)	30.4 (+2.1)	4.6 (+0.5)
CD	25.3 (−0.6)	18.0 (−1.5)	3.9 (+0.6)	32.0 (−0.4) *	24.0 (−0.3) *	4.2 (+0.5)
KU	230.9 (−36.6)	212.3 (−36.7)	7.0 (+1.4)	239.7 (−52.6)	219.2 (−52.1)	7.4 (+2.0)
KD	181.7 (−17.9)	150.3 (−17.0)	15.2 (+0.6)	156.7 (−26.4)	131.6 (−25.3)	11.8 (−0.2) *
OU	30.3 (−3.2)	26.1 (−3.6)	2.3 (+0.4)	43.7 (−2.6)	37.2 (−3.0)	3.7 (+0.3)
OD	46.5 (−5.5)	39.1 (−4.7)	3.2 (−0.2)	52.4 (−2.9)	42.3 (−2.7)	4.5 (0.0) *

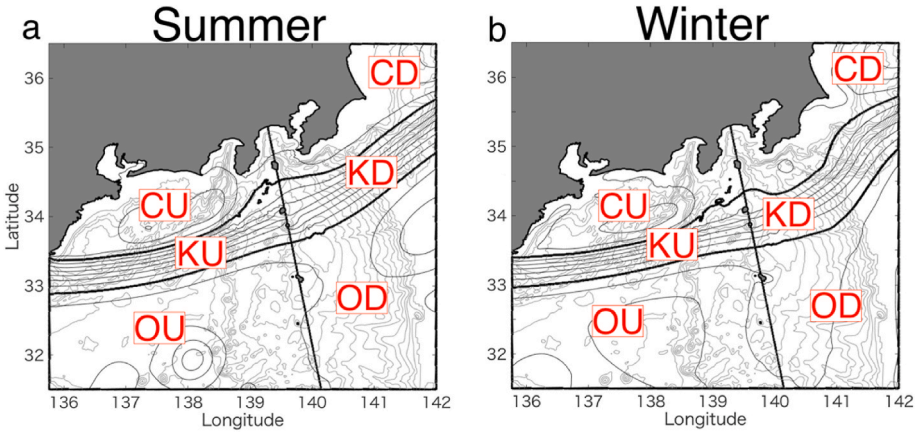

Fig. 9. Six separate regions used for kinetic energy budget analysis in (a) summer (Run #1) and (b) winter (Run #3). Abbreviations: CU, coastal upstream; CD, coastal downstream; KU, Kuroshio upstream; KD, Kuroshio downstream; OU, offshore upstream; OD, offshore downstream.

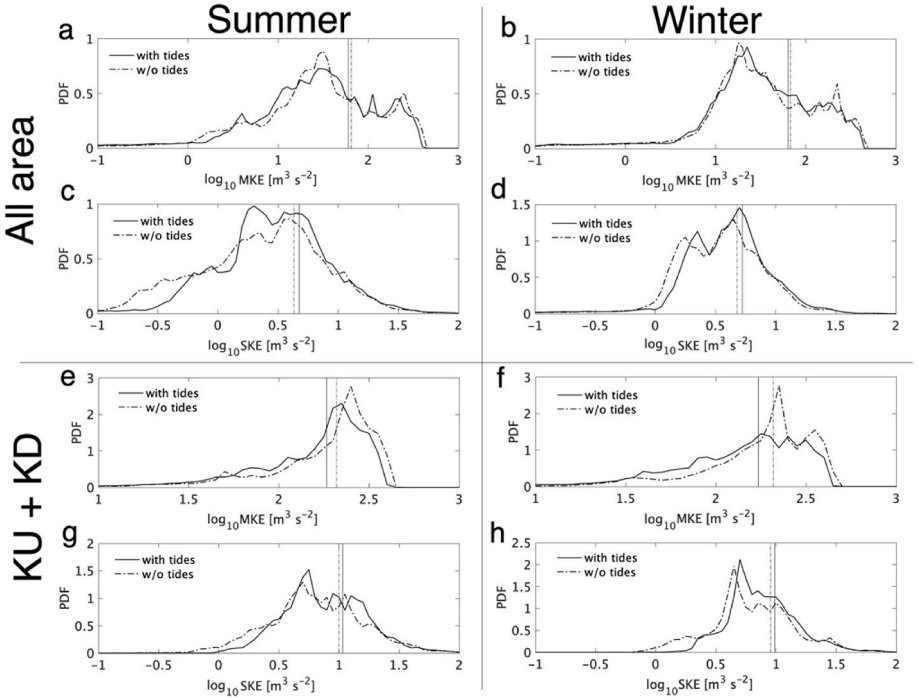

Fig. 10. Probability density functions (PDFs) of (a, b, e, f) mean kinetic energy (MKE) and (c, d, g, h) submesoscale kinetic energy (SKE) in (a–d) for all analyzed areas and along (e–h) the Kuroshio path (upstream, KU, and downstream, KD, regions) for the (left panels) summer and (right panels) winter model cases. Vertical black solid and chain-dotted lines show means for the model cases with and without (w/o) tidal forcing, respectively.

forcing, we compared the probability density functions (PDFs) of the time-averaged and vertically integrated MKE and SKE (Fig. 10). The PDFs of SKE shift to the higher energy side owing to tidal forcing; in particular, the densities at the lower energy tails of SKE are reduced in the cases with tidal forcing (Fig. 10cd). Although modulations of MKEs are not clear from the data in the entire analysis domain, the PDFs of MKEs are clearly shifted to the lower energy side by tidal forcing in the KU and KD regions (Fig. 10ef). According to the Kolmogorov–Smirnov test, the PDFs of the SKE and MKE for the six separate regions are significantly different between model cases with and without tidal forcing ($p < 0.01$). These results imply that tidal forcing significantly modulates the distribution of the SKE and MKE.

3.4. SKE budget

The turbulent kinetic energy (TKE) budget equation in a time domain is generally represented as follows (e.g., Gula et al., 2016b; Wang et al., 2018),

$$\frac{\partial}{\partial t}\frac{\overline{\mathbf{u}'^2_h}}{2} = -\nabla\left(\overline{\mathbf{u}\cdot\frac{\mathbf{u}'^2_h}{2}}\right) - \frac{1}{\rho_0}\nabla(\overline{\mathbf{u}'p'}) - \overline{\mathbf{u}'_h\cdot(\mathbf{u}'\cdot\nabla)\overline{\mathbf{u}}_h} - \frac{g\overline{\rho' w'}}{\rho_0} + \varepsilon \tag{5}$$

where p is pressure, ρ is density, ρ_0 is the reference density of 1027.5 kg m^{-3}, g is the gravitational acceleration, and h denotes the horizontal operator. The overbar and prime indicate time-averaged and fluctuation components in a time domain. The first and second terms on the right-hand side are the advection of SKE by total flows and submesoscale pressure flux terms, respectively. The third and fourth terms on the right-hand side represent shear production and buoyancy production, respectively; that is, energy conversion from MKE to SKE (K_MK_S) and from submesoscale potential energy to SKE (P_SK_S), respectively. These two terms, K_MK_S and P_SK_S, are often referred to as barotropic (BT) conversion and baroclinic (BC) conversion, respectively (e.g., Dong et al., 2007). The last term is the energy sink/dissipation term (viz., viscous effects) including the wind stress (surface drag), interior dissipation and bottom drag. We applied this general TKE equation to our spatially (Gaussian) filtered model output and estimated the SKE budget. The shear production (K_MK_S) and buoyancy production (P_SK_S) terms are expressed as follows:

$$K_MK_S = -\overline{\mathbf{u}_{Sh}\cdot(\mathbf{u}_S\cdot\nabla)\mathbf{u}_{Mh}} \tag{6}$$

$$P_SK_S = -\frac{g\overline{\rho_S w_S}}{\rho_0} \tag{7}$$

The SKE flux (F_{SKE}) and submesoscale pressure flux (F_{SP}) are given by:

$$F_{SKE} = \overline{\mathbf{u}\cdot\frac{\mathbf{u}^2_{S_h}}{2}} \tag{8}$$

$$F_{SP} = \frac{\overline{\mathbf{u}_{S_h}p_S}}{\rho_0} \tag{9}$$

Under a steady-state condition (i.e., $\partial\overline{\mathbf{u}_{S_h}^2}/2\partial t \sim 0$), the dissipation term can be written as follows:

$$\varepsilon = \nabla\cdot F_{SKE} + \nabla\cdot F_{SP} - K_MK_S - P_SK_S \tag{10}$$

where a negative ε indicates net dissipation in the model. Strictly speaking, $\partial\overline{\mathbf{u}_{S_h}^2}/2\partial t$ is not zero during the analysis periods ($\partial\overline{\mathbf{u}_{S_h}^2}/2\partial t = -2.2\times10^{-7}$, -4.8×10^{-7}, 2.1×10^{-7}, and 1.5×10^{-7} m^3s^{-3} for Runs #1–4, respectively. However, these changes in SKE are approximately one to two orders of magnitude smaller than the estimated dissipation. Therefore, we assume that $\partial\overline{\mathbf{u}_{S_h}^2}/2\partial t = 0$ to estimate the dissipation. The cross term associated with K_C is ignored in the SKE budget analysis.

High K_MK_S appears in the vicinity of the islands along the Kuroshio path, and the distribution of the K_MK_S is similar for the summer and winter seasons (Fig. 11a and b). At the same time, P_SK_S shows negative conversion near the islands, although P_SK_S is enhanced in offshore

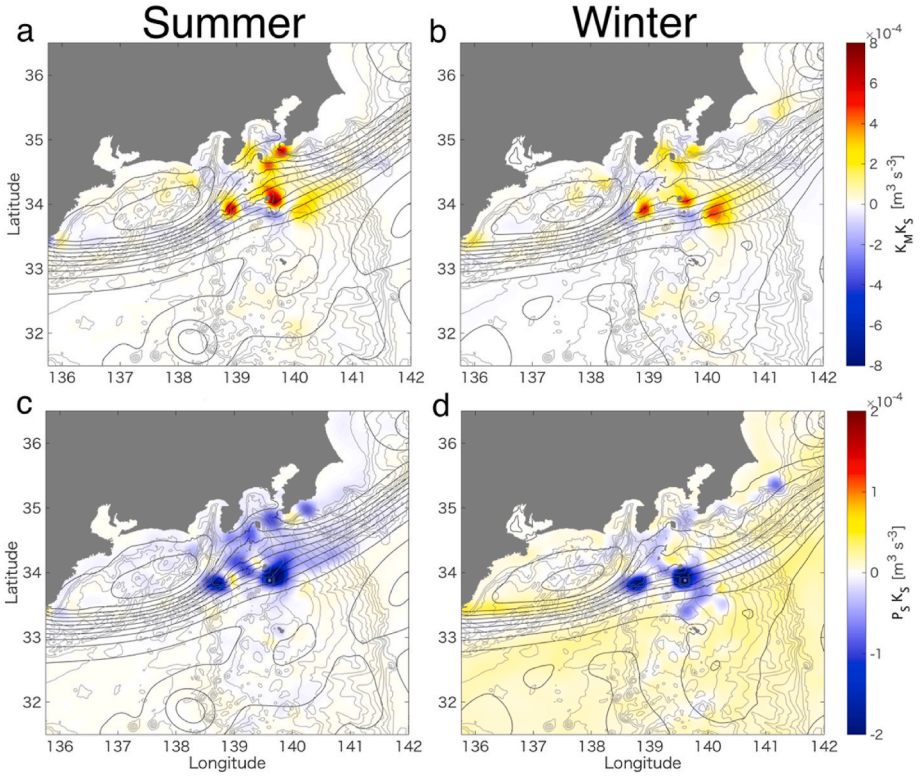

Fig. 11. Time-averaged and depth-integrated (a, b) shear production (K_MK_S) and (c, d) buoyancy production (P_SK_S) for the (a, c) summer and (b, d) winter model cases with tidal forcing. For visualization purposes, the plotted data were smoothed using a horizontal Gaussian filter.

regions in winter (Fig. 10c and d). This enhanced P_SK_S in the winter season is thought to be due to instability resulting from surface winter cooling (Sasaki et al., 2014; Uchiyama et al., 2017). Recent studies of Yang et al. (2021a; 2021b) investigated details of vertical eddy heat transport in the Kuroshio extension in winter. They suggested that the buoyancy flux ($\sim P_SK_S$) is promoted by strong turbulent mixing owing to strong surface cooling with intensified winds through a strong ageostrophic secondary circulation. The strongly enhanced K_MK_S and negative P_SK_S around the islands are consistent with the numerical simulation conducted by Dong et al. (2007). The distributions of the K_MK_S and P_SK_S are not largely altered by tidal forcing (data not shown).

The time-averaged and depth-integrated F_{SKE} and F_{SP} values for the summer are plotted in Fig. 12. The SKE is mainly advected by the eastward Kuroshio and is enhanced near islands over the ridge from O (10) to O (10^2) m^4 s^{-3} (Fig. 12a and b). The divergence of the F_{SKE} near the islands is consistent with that of the K_MK_S, as shown in Fig. 11a. The direction of the submesoscale pressure flux is mainly westward and opposite to that of the Kuroshio and F_{SP} (Fig. 12c and d). The distributions of F_{SKE} and F_{SP} are not largely different between the summer and winter (data not shown). The submesoscale pressure flux should not be caused by barotropic motions, but is thought to be caused by internal gravity waves. Masunaga et al. (2018) reported that internal waves contribute 10% of the total kinetic energy in the study area. The numerical simulations conducted by Rocha et al. (2016) showed that internal gravity waves influence SMs. High F_{SP} areas appear near the Kuroshio path for both model cases, with and without tides (Fig. 12c and d). One possible explanation for the high F_{SP} without tides is near-inertial internal waves (NIIWs) generated by the interaction between background flows and topography (e.g., Waterman et al., 2013; Nagai et al., 2017). Furthermore, frontal instabilities in geostrophic flows can transform energy into NIIW energy via spontaneous generation (e.g., Nagai et al., 2015; Alford et al., 2016). On the other hand, tidal forcing significantly enhances the F_{SP} on the southwest side of the ridge, which is thought to be due to the propagation of internal tides (compare Fig. 12c and d; between 138°E and 140°E). Therefore, the enhanced SKE on the southwest side of the ridge, shown in Fig. 7f, is probably caused by internal tides. The intensity of the internal tide energy flux ranges from approximately 1 to 5 m^4 s^{-3} (Masunaga et al., 2018, 2020), which is similar to the submesoscale pressure flux estimated in our model (Fig. 12c, d, O (1–10) m^4 s^{-3}).

The area- and time-averaged and depth-integrated SKE budgets are shown in Table 4 (with area averaging over the entire analysis domain shown by the black chain-dotted box in Fig. 1b). K_MK_S and P_SK_S are positive and negative in summer, respectively. Approximately half of the SKE generated by K_MK_S is converted back to submesoscale potential energy via negative P_SK_S during summer. The negative buoyancy production can be explained by a highly stratified condition in summer, leading to the suppression of the SKE. In the winter season, K_MK_S is approximately 20% smaller than that in summer, and P_SK_S is positive and comparable with that of K_MK_S.

According to these results, the generation mechanisms of SKE are different in summer and winter, as follows: (1) for the summer season, shear production dominates SKE generation, and buoyancy production suppresses SKE through negative conversion; (2) for the winter season, both shear and buoyancy production equally dominate in SKE

Table 4
Submesoscale kinetic energy budgets. Area- and time-averaged and vertically-integrated $\nabla\cdot F_{SKE}$, $\nabla\cdot F_{SP}$, K_MK_S, P_SK_S, and ε for all model cases (unit = 10^{-7} m^3 s^{-3}). Asterisks denote differences between models with and without tidal forcing that are not significant (t-test, $p > 0.01$).

		$\nabla\cdot F_{SKE}$	$\nabla\cdot F_{SP}$	K_MK_S	P_SK_S	ε
Summer	w/o tides (Run #1)	−1.6	−0.6	105.4	−47.8	−59.9
	with tides (Run #2)	0.4	6.3	112.3	−58.3	−47.4
Winter	w/o tides (Run #3)	−3.6	−0.04 *	78.4	97.1	−179.2
	with tides (Run #4)	−0.9	0.8 *	89.0	79.4	−168.5

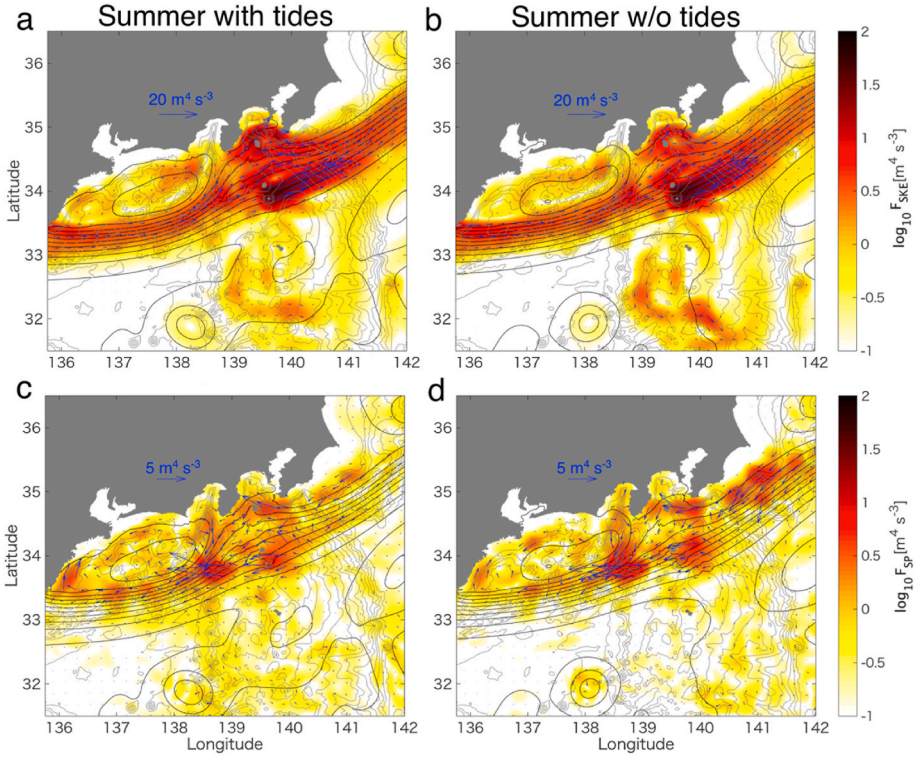

Fig. 12. Time-averaged and depth-integrated (a, b) submesoscale kinetic energy (SKE) flux (F_{SKE}) and (c, d) submesoscale pressure flux (F_{SP}) for the summer model cases (a, c) with and (b, d) without tidal forcing. For visualization purposes, the plotted data were smoothed using a horizontal Gaussian filter.

generation. K_MK_S and P_SK_S increases and decreases with tidal forcing by 7% and 14%, respectively, in summer, and by 22% and 18%, respectively, in winter (these differences are statistically significant (t-test, $p < 0.01$). The enhancement of K_MK_S owing to tides can be explained by lateral shear flows through the interaction between tidal flows and topography. One possible reason for the reduction in P_SK_S owing to tides is tidal mixing. In addition, the buoyancy production might be reduced by energy toward submesoscale internal tides. Indeed, tide-induced and internal tide-induced mixing significantly influence physical processes and transport in the study area (Masunaga et al., 2020). In our model cases, the vertical eddy viscosity computed from the KPP scheme increases by 19% and 8% owing to tidal forcing in summer and winter, respectively. Therefore, tides contribute to the SKE budget in two ways: first by SKE generation through shear production, K_MK_S, and second by the suppression of buoyancy production, P_SK_S, caused by tide-induced mixing.

The divergence of F_{SKE} and F_{SP} is much smaller than that of the other terms, which implies that most of the generated SKE is dissipated in the study area; that is, the SKE budget is mostly closed or balanced. This also implies that intensified mixing due to enhanced SKE mainly influences local transport in the study area. The divergence of F_{SP} in the summer case with tides (Run #2) is significantly higher than that in other cases (Table 4). For the winter season, there is no significant difference in the F_{SP} between model cases with and without tidal forcing (Table 4). The enhanced submesoscale pressure flux of the F_{SP} due to tides in summer should be the baroclinic pressure flux (internal tide energy flux) because the wavelength of barotropic tidal waves is O (10^3) km and cannot be exhibited as a small-scale submesoscale component. Therefore, the intensified divergence of F_{SP} caused by tides represents internal tide generation and propagation, which enhances the radiation of SKE far from internal tide-generation sites.

The dissipation and sink of the SKE varies seasonally. During the summer season, SKE sinks via two pathways: approximately half of the SKE from shear production sinks to negative potential energy production (P_SK_S) and the other half sinks as dissipation. During the winter season, most of the SKE generated owing to shear and buoyancy production sinks into dissipation. Based on our modeling, winter dissipation is approximately three times higher than that in the summer and is weakened by tidal forcing owing to negative buoyancy production (P_SK_S) by tides.

4. Conclusions

This study investigated submesoscale kinetic energy (SKE) and associated transport using a double-nested downscaled ROMS in the vicinity of the Izu-Ogasawara Ridge located off mainland Japan. SKE induced by submesoscale coherent structures (SMs) at scales of less than ~45 km was extracted using a horizontal Gaussian filter with a filter length of 9 km. Based on our results, tidal forcing intensifies the SKE via shear production owing to mean currents. In contrast, the MKE is suppressed by tides through tidally-induced dissipation. SKE budgets vary seasonally; in summer, SKE generated by the shear production sinks into submesoscale potential energy (negative buoyancy production) and energy dissipation; in winter, SKE is generated by both shear and buoyancy production and sinks into energy dissipation.

SMs are important for understanding the physical processes and mass fluxes that maintain oceanic ecosystems (Mahadevan, 2016; McWilliams, 2016). Western boundary currents, such as the Kuroshio and Gulf stream, significantly influence SMs (e.g., Sasaki et al., 2014; Gula et al., 2016a) and are important contributors to the transport of heat (Jayne et al., 2002), nutrients (Guo et al., 2013), and fish larvae (Rypina et al., 2014; Chang et al., 2018). Our study provides new insights into the interactions between western boundary currents, SMs, and tides. Overall, our work shows that SMs are enhanced by tides, whereas the background mean kinetic energy caused by the Kuroshio is suppressed by tides. We suggest that tides and associated SMs should therefore be further considered to fully understand physical and ecosystem processes and dynamics in the North Pacific. This study reveals the effects of tides on the kinetic energy budget and SMs; however, internal tides were not separated by our filtering approach using a horizontal Gaussian filter. To further investigate the effects of tides and internal tides on SMs, more advanced filtering techniques for both the temporal and spatial domains are needed (e.g., Torres et al., 2018).

Declaration of competing interest

The authors declare that they have no known competing financial interests or personal relationships that could have appeared to influence the work reported in this paper.

Data availability

Data will be made available on request.

Acknowledgements

This study was supported by a JSPS Grant-in-Aid for Scientific Research (18H03798, 19K20432 and 22K18018). E. Masunaga also acknowledges a grant from the Fundamental Research Developing Association for Shipbuilding and Offshore (REDAS).

References

Alford, M.H., et al., 2015. The formation and fate of internal waves in the South China Sea. Nature 521 (7550), 65–69.
Alford, M.H., MacKinnon, J.A., Simmons, H.L., Nash, J.D., 2016. Near-inertial internal gravity waves in the ocean. Annu. Rev. Mar. Sci. 8, 95–123.
Andres, M.S., Jan, T.B., Sanford, V., Mensah, L.R., Centurioni, Book, J.W., 2015. Mean structure and variability of the Kuroshio from northeastern Taiwan to southwestern Japan. Oceanography 28 (4), 84–95.
Becker, J.J., et al., 2009. Global bathymetry and elevation data at 30 arc seconds resolution: SRTM30_PLUS. Mar. Geodes. 32–4, 355–371.
Boccaletti, G., Ferrari, R., Fox-Kemper, B., 2007. Mixed layer instabilities and restratification. J. Phys. Oceanogr. 37 (9), 2228–2250.
Capet, X., McWilliams, J.C., Molemaker, J.M., Shchepetkin, A.F., 2008. Mesoscale to submesoscale transition in the California Current System. Part I: flow structure, eddy flux, and observational tests. J. Phys. Oceanogr. 38, 29–43.
Carter, G.S., et al., 2008. Energetics of M2 barotropic-to-baroclinic tidal conversion at the Hawaiian Islands. J. Phys. Oceanogr. 38 (10), 2205–2223.
Chang, Y.L.K., Miller, M.J., Tsukamoto, K., Miyazawa, Y., 2018. Effect of larval swimming in the western North Pacific subtropical gyre on the recruitment success of the Japanese eel. PLoS One 13 (12), e0208704.
Cheng, Y.H., et al., 2020. Submesoscale eddy and frontal instabilities in the Kuroshio interacting with a cape south of Taiwan. J. Geophys. Res.: Oceans 125 (5) e2020JC016123.
Dauhajre, D.P., McWilliams, J.C., 2018. Diurnal evolution of submesoscale front and filament circulations. J. Phys. Oceanogr. 48 (10), 2343–2361.
Dong, C., McWilliams, J.C., Shchepetkin, A.F., 2007. Island wakes in deep water. J. Phys. Oceanogr. 37 (4), 962–981.
Egbert, G.D., Erofeeva, S.Y., 2002. Efficient inverse modeling of barotropic ocean tides. J. Atmos. Ocean. Technol. 19, 183–204.
Gula, J., Molemaker, M.J., McWilliams, J.C., 2016a. Submesoscale dynamics of a Gulf stream frontal eddy in the South Atlantic Bight. J. Phys. Oceanogr. 46 (1), 305–325.
Gula, J., Molemaker, M.J., McWilliams, J.C., 2016b. Topographic generation of submesoscale centrifugal instability and energy dissipation. Nat. Commun. 7 (1), 1–7.
Guo, X.Y., Zhu, X.H., Long, Y., Huang, D.J., 2013. Spatial variations in the Kuroshio nutrient transport from the East China Sea to south of Japan. Biogeosciences 10 (10), 6403–6417.
Hasegawa, D., Yamazaki, H., Lueck, R.G., Seuront, L., 2004. How islands stir and fertilize the upper ocean. Geophys. Res. Lett. 31 (16).
Jayne, S.R., Marotzke, J., 2002. The oceanic eddy heat transport. J. Phys. Oceanogr. 32 (12), 3328–3345.
Kamidaira, Y., Uchiyama, Y., Mitarai, S., 2017. Eddy-induced transport of the Kuroshio warm water around the Ryukyu islands in the East China sea. Continent. Shelf Res. 143, 206–218.
Kamidaira, Y.Y., Uchiyama, H., Kawamura, T., Kobayashi, Furuno, A., 2018. Submesoscale mixing on initial dilution of radionuclides released from the Fukushima Daiichi nuclear power plant. J. Geophys. Res.: Oceans 123 (4), 2808–2828.
Kang, D., Fringer, O.B., 2012. Energetics of barotropic and baroclinic tides in the Monterey Bay area. J. Phys. Oceanogr. 42 (2), 272–290.

Kimura, S.A., Kasai, H., Nakata, T., Sugimoto, J.H., Simpson, J.V., Cheok, 1997. Biological productivity of meso-scale eddies caused by frontal disturbances in the Kuroshio. ICES (Int. Counc. Explor. Sea) J. Mar. Sci. 54 (2), 179–192.
Kodama, T.Y., Shimizu, T., Ichikawa, Y., Hiroe, A., Kusaka, H., Morita, M., Shimizu, Hidaka, K., 2014. Seasonal and spatial contrast in the surface layer nutrient content around the Kuroshio along 138 E, observed between 2002 and 2013. J. Oceanogr. 70 (6), 489–503.
Large, W.G., McWilliams, J.C., Doney, S.C., 1994. Oceanic vertical mixing: a review and a model with a nonlocal boundary layer parameterization. Rev. Geophys. 32, 363–403.
Lévy, M.R., Ferrari, P.J., Franks, A.P., Martin, Rivière, P., 2012. Bringing physics to life at the submesoscale. Geophys. Res. Lett. 39 (14).
Liu, C.L., Chang, M.H., 2018. Numerical studies of submesoscale island wakes in the Kuroshio. J. Geophys. Res.: Oceans 123 (8), 5669–5687.
Mahadevan, A., 2016. The impact of submesoscale physics on primary productivity of plankton. Ann. Rev. Mar. Sci 8, 161–184.
Mason, E.J., Molemaker, A.F., Shchepetkin, F., Colas, J.C., McWilliams, Sangrà, P., 2010. Procedures for offline grid nesting in regional ocean models. Ocean Model. 35 (1), 1–15.
Masunaga, E., Arthur, R.S., Fringer, O.B., 2019b. Internal Wave Breaking Dynamics and Associated Mixing in the Coastal Ocean. Encyclopedia of Ocean Science, pp. 548–554.
Masunaga, E., Fringer, O.B., Kitade, Y., Yamazaki, H., Gallager, S.M., 2017. Dynamics and energetics of trapped diurnal internal Kelvin waves around a midlatitude island. J. Phys. Oceanogr. 47 (10), 2479–2498.
Masunaga, E., Uchiyama, Y., Suzue, Y., Yamazaki, H., 2018. Dynamics of internal tides over a shallow ridge investigated with a high-resolution downscaling Regional Ocean model. Geophys. Res. Lett. 45 (8), 3550–3558.
Masunaga, E., Uchiyama, Y., Yamazaki, H., 2019. Strong internal waves generated by the interaction of the Kuroshio and tides over a shallow ridge. J. Phys. Oceanogr. 49 (11), 2917–2934.
Masunaga, E., Arthur, R.S., Yamazaki, H., 2020. Baroclinic residual circulation and mass transport due to internal tides. J. Geophys. Res.: Oceans. https://doi.org/10.1029/2019JC015316.
McWilliams, J.C., 2016. Submesoscale currents in the ocean. Proc. Roy. Soc. A. Math. Phys. Eng. Sci. vol. 472 (2189), 20160117.
Miyake, Y., Tellier, M.A.A., Takeshige, H., Itakura, A., Yoshida, A., Kimura, S., 2020. Past and lost influence of the Kuroshio on estuarine recruitment of Anguilla japonica glass eels. J. Oceanogr. 1–12.
Miyazawa, Y., Zhang, R., Guo, X., Tamura, H., Ambe, D., Lee, J., Okuno, A., Yoshinari, H., Setou, T., Komatsu, K., 2009. Water mass variability in the Western North Pacific detected in 15-year eddy resolving ocean reanalysis. J. Oceanogr. 65, 737–756.
Nagai, T., Tandon, A., Kunze, E., Mahadevan, A., 2015. Spontaneous generation of near-inertial waves by the Kuroshio Front. J. Phys. Oceanogr. 45 (9), 2381–2406.
Nagai, T.D., Hasegawa, T., Tanaka, H., Nakamura, E., Tsutsumi, R., Inoue, Yamashiro, T., 2017. First evidence of coherent bands of strong turbulent layers associated with high-wavenumber internal-wave shear in the upstream Kuroshio. Sci. Rep. 7 (1), 1–14.
Nakamura, T., Matthews, J.P., Awaji, T., Mitsudera, H., 2012. Submesoscale eddies near the Kuril Straits: asymmetric generation of clockwise and counterclockwise eddies by barotropic tidal flow. J. Geophys. Res.: Oceans 117 (C12).
Nakata, H., Kimura, S., Okazaki, Y., Kasai, A., 2000. Implications of meso-scale eddies caused by frontal disturbances of the Kuroshio Current for anchovy recruitment. ICES J. Mar. Sci. 57 (1), 143–152.
Omand, M.M., D'Asaro, E.A.C.M., Lee, M.J., Perry, N., Briggs, I., Cetinić, I., Mahadevan, A., 2015. Eddy-driven subduction exports particulate organic carbon from the spring bloom. Science 348 (6231), 222–225.
Roads, J., 2004. Experimental weekly to seasonal US forecasts with the regional spectral model. Bull. Am. Meteorol. Soc. 85 (12), 1887–1902.
Rocha, C.B., Gille, S.T., Chereskin, T.K., Menemenlis, D., 2016. Seasonality of submesoscale dynamics in the Kuroshio extension. Geophys. Res. Lett. 43 (21), 11–304.
Rypina, I.I., Llopiz, J.K., Pratt, L.J., Lozier, M.S., 2014. Dispersal pathways of American eel larvae from the Sargasso Sea. Limnol. Oceanogr. 59 (5), 1704–1714.
Sasaki, H., Klein, P., Qiu, B., Sasai, Y., 2014. Impact of oceanic-scale interactions on the seasonal modulation of ocean dynamics by the atmosphere. Nat. Commun. 5 (1), 1–8.
Shchepetkin, A.F., McWilliams, J.C., 2005. The regional oceanic modeling system (ROMS): a split-explicit, free-surface, topography-following-coordinate oceanic model. Ocean Model. 9 (4), 347–404.
Su, Z., Wang, J., Klein, P., Thompson, A.F., Menemenlis, D., 2018. Ocean submesoscales as a key component of the global heat budget. Nat. Commun. 9 (1), 1–8.
Thomas, L.N., Tandon, A., Mahadevan, A., 2008. Submesoscale processes and dynamics. Ocean Model. Eddying Regime 177, 17–38.
Torres, H.S., et al., 2018. Partitioning ocean motions into balanced motions and internal gravity waves: a modeling study in anticipation of future space missions. J. Geophys. Res.: Oceans 123 (11), 8084–8105.
Tsutsumi, E., Matsuno, T., Lien, R.C., Nakamura, H., Senjyu, T., Guo, X., 2017. Turbulent mixing within the K uroshio in the T okara S trait. J. Geophys. Res.: Oceans 122 (9), 7082–7094.
Uchiyama, Y., Suzue, Y., Yamazaki, H., 2017. Eddy-driven nutrient transport and associated upper-ocean primary production along the Kuroshio. J. Geophys. Res.: Oceans 122, 5046–5062.
Uchiyama, Y.S., Odani, M., Kashima, Y., Kamidaira, Mitarai, S., 2018. Influences of the Kuroshio on interisland remote connectivity of corals across the Nansei archipelago in the East China sea. J. Geophys. Res.: Oceans 123 (12), 9245–9265.
Varlamov, S.M., Guo, X., Miyama, T., Ichikawa, K., Waseda, T., Miyazawa, Y., 2015. M2 baroclinic tide variability modulated by the ocean circulation south of Japan. J. Geophys. Res.: Oceans 120 (5), 3681–3710.
Wang, Y., Stewart, A.L., 2018. Eddy dynamics over continental slopes under retrograde winds: insights from a model inter-comparison. Ocean Model. 121, 1–18.
Waseda, T.H., Mitsudera, B., Taguchi, Yoshikawa, Y., 2003. On the eddy-Kuroshio interaction: meander formation process. J. Geophys. Res.: Oceans 108 (C7).
Waterman, S, Garabato, A.C.N., Polzin, K.L., 2013. Internal waves and turbulence in the Antarctic Circumpolar Current. J. Phys. Ocean. 43 (2), 259–282.
Woodruff, S.D., Slutz, R.J., Jenne, R.L., Steurer, P.M., 1987. A comprehensive ocean-atmosphere data set. Bull. Am. Meteorol. Soc. 68 (10), 1239–1250.
Yang, P.Z., Jing, B., Sun, L., Wu, B., Qiu, P., Chang, Ramachandran, S., 2021a. On the upper-ocean vertical eddy heat transport in the Kuroshio extension. Part I: variability and dynamics. J. Phys. Oceanogr. 51 (1), 229–246.
Yang, P.Z., Jing, B., Sun, L., Wu, B., Qiu, P., Chang, S., Ramachandran, Yuan, C., 2021b. On the upper-ocean vertical eddy heat transport in the Kuroshio extension. Part II: effects of air–sea interactions. J. Phys. Oceanogr. 51 (10), 3297–3312.